

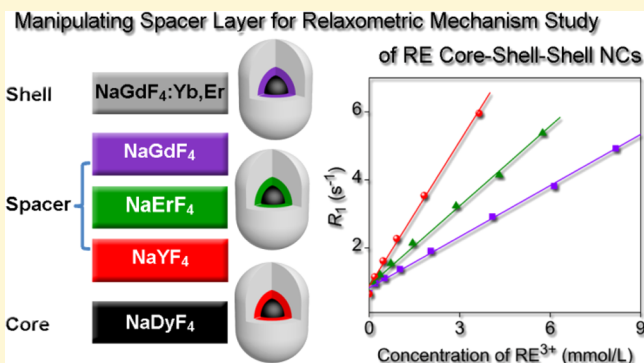
Chemical Spacer Design for Engineering the Relaxometric Properties of Core–Shell Structured Rare Earth Nanoparticles

Jiayi Huang, Yi Hou, Chunyan Liu,* Lihong Jing, Tiancong Ma, Xiaodan Sun, and Mingyuan Gao*

Institute of Chemistry, Chinese Academy of Sciences, Bei Yi Jie 2, Zhong Guan Cun, Beijing 100190, China

Supporting Information

ABSTRACT: The development of T_1/T_2 dual-modality contrast agents for magnetic resonance imaging (MRI) is beneficial for eliminating artifacts. However, T_1 and T_2 agents in the case of direct contact will interfere with each other, and the intrinsic mechanism remains unclear yet. Gadolinium(III) is widely used as T_1 contrast agents, while dysprosium(III) exhibits the strongest magnetic moment among rare earth (RE) elements due to the spin–orbital coupling and can potentially be used as T_2 contrast agents. The very similar chemical properties of RE elements allow integration of Gd(III) and Dy(III) within single nanocrystals for investigating the interactions between T_1 and T_2 components so as to achieve T_1/T_2 dual-modality contrast agents with optimized performance. Therefore, core–shell–shell structured $\text{NaDyF}_4@(\text{NaREF}_4)_2@(\text{NaGdF}_4)_2$ nanocrystals were prepared via a seed-mediated growth approach and Gd(III), Er(III), and Y(III) were chosen to construct NaREF_4 spacer layer for mediating the interactions between Dy(III) and Gd(III) ions. It was found out that, with the decrease of the electron cloud distortion ability from Gd(III) to Y(III), the PEGylated core–shell–shell particles present increasing longitudinal relaxivity values from 0.50 to $1.82 \text{ mM}^{-1} \text{ s}^{-1}$. On the basis of the longitudinal relaxivity theory and polarizability of different RE elements, the above tendency can be interpreted by the distortion tendency of the electron cloud of RE(III) in the spacer layer which strongly mediates the interactions between electron clouds of Dy(III) and Gd(III) ions. Further upconversion luminescence spectroscopy study in combination with the relaxivity measurements on nanocrystals with thicker spacer (3.5 vs 1.9 nm) also supported the above explanation.



INTRODUCTION

Magnetic resonance imaging (MRI) has been recognized as a powerful imaging tool to acquire detailed internal structures of body with high spatial resolution and unlimited tissue penetration in a noninvasive manner. However, MRI contrast agents are often required for better distinguishing malignant tumor tissues from normal tissues in cancer diagnosis.^{1,2} Clinical scanner determines the water proton relaxation that is characterized by longitudinal (spin–lattice) relaxation time (T_1) and transverse (spin–spin) relaxation time (T_2). The MRI contrast agents do not provide MR signal but effectively shorten the T_1 or T_2 of water protons in tissues where they present. The MRI contrast agents can roughly be classified into two groups, that is, positive contrast agents (T_1 agents) and negative contrast agents (T_2 agents). The former gives rise to hyperintensive signal while the latter produces hypointensive signal.^{3,4} Until now, T_1 agents are dominated by various types of paramagnetic Gd chelates that have been largely used in the clinic, while T_2 agents mainly refer to superparamagnetic iron oxide nanoparticles that remain mostly in preclinical stages.⁵

Dual-modality MR imaging combining both T_1 and T_2 modalities can provide complementary diagnostic information and eliminate the artifacts resulting from the single modality

imaging owing to their intrinsic limitations.^{6–8} Some magnetic materials, such as ultrasmall iron oxide nanoparticles and FeCo nanoparticles, simultaneously exhibit contrast enhancement effects for T_1/T_2 dual-modality imaging owing to their intrinsic properties.^{9,10} However, properly balancing the T_1 and T_2 contrast enhancement effects remains challenging.¹¹

An alternative approach to achieve T_1/T_2 dual-modality contrast agents is to integrate T_1 and T_2 components through covalent or noncovalent conjugation approaches, which is applicable for combining paramagnetic metal chelates with iron oxide nanoparticles. However, the relaxation process of paramagnetic T_1 contrast agents is easily perturbed by the magnetic field generated from superparamagnetic T_2 contrast materials.⁶ For example, loading Gd³⁺ chelates in the mesoporous silica shell of Fe₃O₄ nanoparticles led to negligible longitudinal relaxivity r_1 although the transverse relaxivity r_2 was largely increased.¹² In contrast, another study revealed that the transverse relaxivity r_2 of iron oxide particles was decreased when Gd-diethylenetriamine pentaacetate was attached to the

Received: July 27, 2015

Revised: November 5, 2015

Published: November 6, 2015

surface of Fe_3O_4 particles coated with SiO_2 ,¹³ suggesting that T_1 component may also alter the performance of T_2 component though the underlying mechanism remains unclear.

In fact, the relaxometric properties of magnetic nanoparticles are largely affected by their colloidal dispersity in aqueous solution. Therefore, integrating T_1 and T_2 components in single nanocrystals is helpful to rule out the influence of surface attachment of T_1 agent on the colloidal stability and aggregation state of the resulting particles in solution, so as to clarify the intrinsic interference between T_1 and T_2 components. Rare earth (RE) elements, rich in magnetic properties that benefitted from their unique 4f electron configurations, provide such an opportunity. For example, Gd^{3+} possesses the largest number of unpaired f electrons and is the optimal choice for constructing Gd-chelate-based T_1 contrast agents.^{14–16} However, recent studies have demonstrated that Gd-containing inorganic nanoparticles such as GdF_3 , Gd_2O_3 , and NaGdF_4 nanoparticles exhibit superior T_1 contrast enhancement effects owing to increased number of Gd^{3+} ions per contrast agent unit.^{17–19} In difference, Dy^{3+} presents the highest magnetic moment arising from the spin–orbital coupling,²⁰ and therefore Dy^{3+} -containing nanoparticles such as NaDyF_4 , Dy_2O_3 , and $\text{Dy}(\text{OH})_3$ show remarkable T_2 contrast enhancement effects.^{21,22} The very similar chemical properties of RE elements enable integration of these two types of ions into single crystals. Moreover, the seed-mediated growth approach provides an excellent opportunity to spatially separate them upon the construction of core–shell nanocrystals, which thus provides an excellent model for investigating the interactions between T_1 and T_2 agents for deeply understanding and optimizing the contrast enhancement performance of T_1/T_2 dual-modality contrast agents.

Following our previous investigations on the preparation of RE nanoparticle-based tumor-specific MR imaging probes and the studies on relaxometric properties of iron oxide nanoparticles,^{11,19,23,24} we herein report core–shell–shell structured $\text{NaDyF}_4@ \text{NaREF}_4@ \text{NaGdF}_4:\text{Yb,Er}$ nanocrystals with RE in spacer layer being varied from Gd^{3+} , to Er^{3+} , to Y^{3+} . The RE elements in the spacer layer were chosen according to their electron cloud distortion ability so as to effectively mediate the interactions between Dy^{3+} and Gd^{3+} .²⁵ Gd^{3+} ions were placed in the outermost layer to facilitate their direct contact with water molecules to induce effective electron–nuclear dipolar interactions. Co-doping of Yb^{3+} and Er^{3+} ions can not only present potential for an alternative buildup of multimodality optical/MR imaging probes but also provide an extra approach to evaluate the mediation. The core–shell–shell nanoparticles were prepared through seed-mediated growth at high temperature upon replacement reactions. The longitudinal relaxivity of differently structured nanoparticles was carefully studied after the resulting nanocrystals were capped with polyethylene glycol (PEG). In combination with related theories, the underlying mechanism governing the performance of T_1 and T_2 contrast enhancement effects was discussed.

EXPERIMENTAL SECTION

Chemicals. The following materials were purchased from Sigma-Aldrich: $\text{DyCl}_3 \cdot 6\text{H}_2\text{O}$ (203173), $\text{GdCl}_3 \cdot 6\text{H}_2\text{O}$ (G7532), $\text{YCl}_3 \cdot 6\text{H}_2\text{O}$ (464317), $\text{YbCl}_3 \cdot 6\text{H}_2\text{O}$ (337927), $\text{ErCl}_3 \cdot 6\text{H}_2\text{O}$ (289256), oleic acid (OA, 364525), 1-octadecene (ODE, O806), and ammonium fluoride (NH_4F , 216011). Analytical-grade chemicals such as NaOH, ethanol, cyclohexane, and tetrahydrofuran (THF) were purchased from Sinopharm Chemical Reagent Beijing, Co., Ltd. The asymmetric

PEG bearing a maleimide group at one end and a diphosphate group at the other (mal-PEG-dp) was a gift from Beijing Oneder Hightech Co., Ltd.

Preparation of $\text{NaDyF}_4@ \text{NaREF}_4@ \text{NaGdF}_4:\text{Yb,Er}$ Nanocrystals. The $\text{NaDyF}_4@ \text{NaREF}_4@ \text{NaGdF}_4:\text{Yb,Er}$ (RE = Gd, Er, Y) core–shell–shell nanocrystals were prepared based on a seed-mediated growth method. First of all, the core of NaDyF_4 nanocrystals were synthesized through a replacement reaction at high temperature according to our previous preparation of NaGdF_4 nanocrystals.²³ In a typical synthesis, 1 mmol of $\text{DyCl}_3 \cdot 6\text{H}_2\text{O}$ were mixed with 16 mL of OA and 16 mL of ODE in a 100 mL flask. The resultant mixture was heated to 150 °C under reduced pressure. After a homogeneous solution was formed, the solution was cooled down to 50 °C, and then 10 mL of methanol solution containing NaOH (2.5 mmol) and NH_4F (4 mmol) was introduced dropwise and the reaction system was then kept under stirring at this temperature for 30 min. Subsequently, methanol was removed by keeping the reaction system at 100 °C for 10 min under vacuum. The reaction mixture was quickly heated to 300 °C within 10 min under nitrogen protection. After 60 min, the reaction was terminated and the reaction mixture was cooled to room temperature. The resultant nanocrystals were precipitated by ethanol, collected by centrifugation, washed with ethanol several times, and finally redispersed in THF or cyclohexane for additional experiments.

A subsequent deposition of a spacer layer of NaREF_4 (RE = Gd, Er, Y) and an outermost layer of $\text{NaGdF}_4:\text{Yb,Er}$ were carried out by first dissolving the core particles in ODE. The following procedures for growing the corresponding shells were the same as those mentioned above for the core preparation.

Ligand Exchange. The water-soluble nanoparticles were prepared via a ligand-exchange reaction following our previous report.²³ Briefly, approximately 10 mg of the purified nanocrystals and 100 mg of mal-PEG-dp were dissolved in 5 mL of THF. The ligand-exchange reaction was kept overnight at room temperature, and then the PEGylated particles were precipitated and washed with cyclohexane three times, and finally dried under vacuum at room temperature. The obtained nanoparticles were dispersed in Milli-Q water after removing the free ligands by ultrafiltration using a 100 kDa filter (Millipore) at 6000g.

Magnetic Relaxivity of PEGylated Particles. The relaxivity measurements were carried out on a 3 T clinical MRI instrument (GE Signa 3.0 T HD, Milwaukee, WI). A series of aqueous solutions with different concentrations of (mal-PEG-dp)-coated particles were prepared and transferred into 1.5 mL Eppendorf tubes for longitudinal and transverse magnetic relaxivity measurements. For T_1 measurements, the parameters were set as follows: echo time (TE) = 25.3 ms; repetition time (TR) = 500, 1000, 1500, and 2000 ms; number of excitations (NEX) = 8. For T_2 measurements, the parameters were set as TR = 2000 ms; TE = 20, 40, 60, 80, and 100 ms, respectively.

Characterization. TEM measurements were carried out with a JEM-100CXII microscope operating at 100 kV for characterizing the particle size and shape. The particle size was determined by counting more than 300 nanoparticles per sample with the aid of ImageJ. The concentration of the RE elements in different samples was determined by using ICP-AES (Thermo ICP 6300) after the particles had been eroded with concentrated hydrochloric acid. The magnetic properties were characterized by using a Quantum Design MPMS-XLS SQUID magnetometer. The upconversion luminescence spectra were recorded on a Cary Eclipse fluorescence spectrophotometer equipped with a 980 nm CW laser diode (0–2 W) serving as extra excitation source. The hydrodynamic sizes of different nanoparticles were characterized by dynamic light scattering (DLS) which was carried out at 298.0 K with a Zetasizer Nano ZS (Malvern) equipped with a solid-state He–Ne laser ($\lambda = 633$ nm).

RESULTS

Structural Characterization of $\text{NaDyF}_4@ \text{NaGdF}_4@ \text{NaGdF}_4:\text{Yb,Er}$ Nanoparticles. The TEM images shown in Figure 1 reveal that the OA-capped core NaDyF_4 , core–shell $\text{NaDyF}_4@ \text{NaGdF}_4$, and core–shell–shell $\text{NaDyF}_4@ \text{NaGdF}_4@ \text{NaGdF}_4:\text{Yb,Er}$ nanocrystals (denoted as samples A_1 , A_2 , and

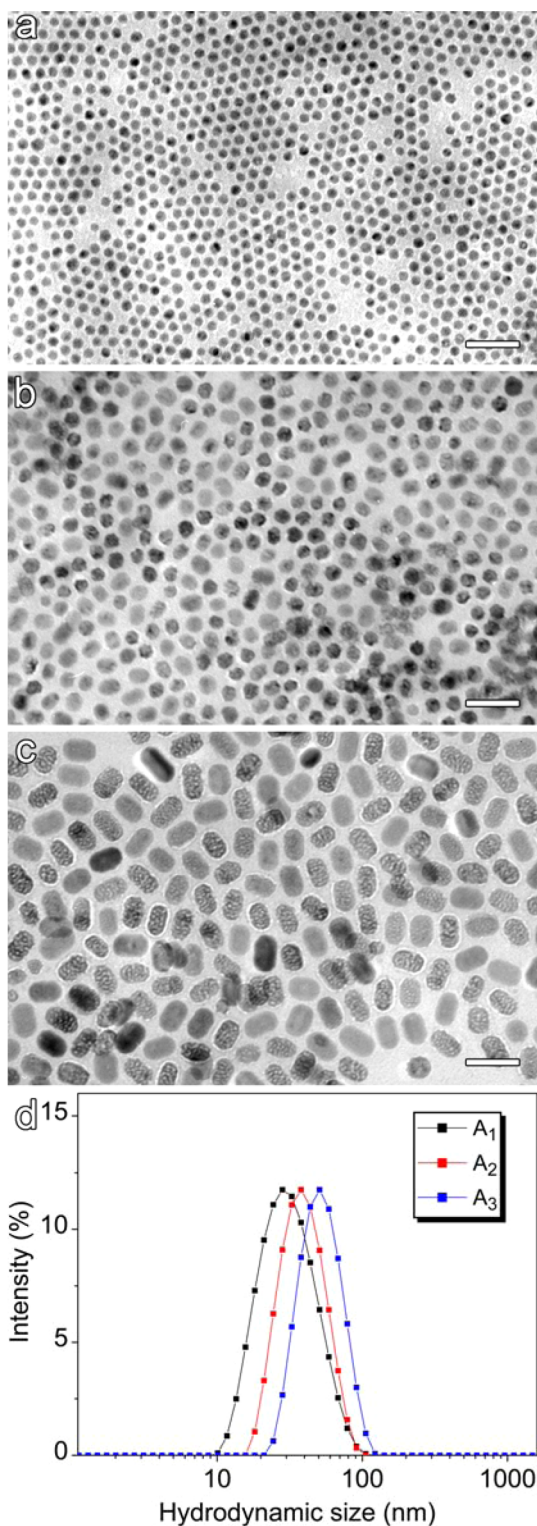


Figure 1. Transmission electron microscopy (TEM) images of NaDyF₄ (a), NaDyF₄@NaGdF₄ (b), and NaDyF₄@NaGdF₄:Yb,Er (c) nanocrystals (denoted as samples A₁, A₂, and A₃). The scale bars embedded in the TEM images correspond to 50 nm. (d) The hydrodynamic size distribution profiles of samples A₁, A₂, and A₃.

A₃) are rather monodispersed and with average sizes of 8.7 ± 1.0 , 14.1 ± 1.5 , and $19.5 \pm 2.1 \times 30.2 \pm 2.6$ nm, respectively. During the shell-coating process, the average sizes of the nanocrystals increase and the shapes change from sphere to

short rod, whereas the monodispersity remains unchanged, indicating no unwanted secondary nucleation occurred. The thickness of the spacer layer was calculated to be 2.7 nm. Furthermore, electron diffractometry studies shown in Figure S1 in Supporting Information revealed that the shell coating did not alter the crystalline structure of the seed crystals, and samples A₁, A₂, and A₃ were all in hexagonal phase.

The as-prepared nanocrystals were hydrophobic since they were stabilized by OA ligands. To obtain water-soluble particles for further relaxivity study, mal-PEG-dp was used to replace the oleate ligand on the surface of nanocrystals based on the fact that the phosphate group has a higher binding affinity to RE³⁺ than the carboxyl group from OA. The aqueous dispersion state of the resultant particles was characterized by DLS analysis (shown in Figure 1d). Samples A₁, A₂, and A₃ all exhibit a relatively narrow particle size distribution in water with a single scattering peak locating at 28.2, 37.8, and 50.7 nm, respectively, which indicates that the ligand-exchange process took place in a controlled way without undesirable agglomeration.

Relaxivity Measurements of PEGylated Particles. The performance of the PEGylated samples as potential MRI contrast agents was evaluated on a clinic 3 T MRI scanner. Since apart from Y³⁺, all the remaining RE elements involved are paramagnetic ions, that is, Dy³⁺, Gd³⁺, Yb³⁺, and Er³⁺, the molar relaxivities r_i ($i = 1, 2$) in this work were extracted from the linear regression fits of the experimental relaxivity R_i ($R_i = 1/T_i$) of water protons against the total molar concentration of all these magnetic RE ions, as shown in Figure 2. The ionic r_1

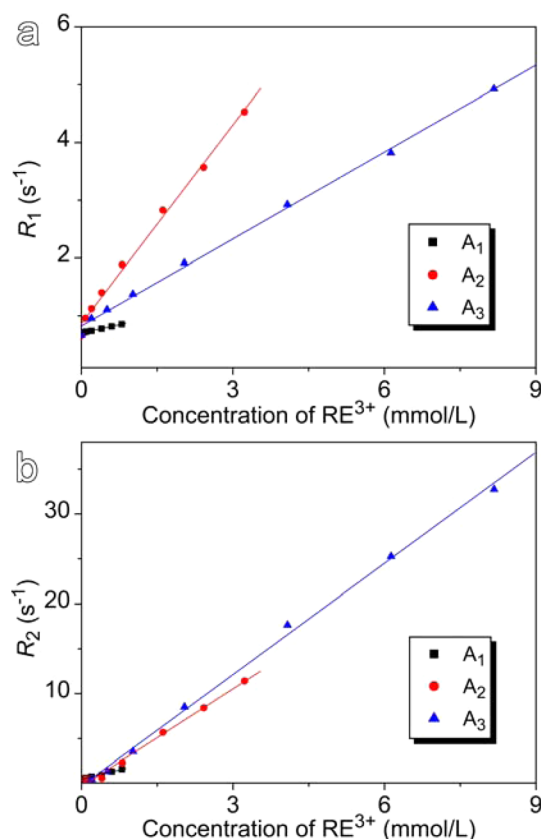


Figure 2. R_1 (a) and R_2 (b) of water protons plotted against the total molar concentration of magnetic RE ions in aqueous solution of samples A₁, A₂, and A₃. The solid lines are their corresponding linear fittings.

value of sample A₁ is almost negligible ($0.19 \text{ mM}^{-1} \text{ s}^{-1}$) due to the short electronic relaxation time of Dy³⁺. However, it is increased to $1.15 \text{ mM}^{-1} \text{ s}^{-1}$ after the deposition of the NaGdF₄ shell due to the presence of Gd³⁺ ions showing higher r_1 value. But the deposition of the following NaGdF₄:Yb,Er shell decreased r_1 value down to $0.5 \text{ mM}^{-1} \text{ s}^{-1}$, which may be attributed to the decreased surface-to-volume ratio as the surface Gd³⁺ ions largely contribute to the r_1 value of the particles. However, the r_1 value of sample A₃ remains much smaller than that of similar-sized NaGdF₄ nanoparticles (denoted as reference sample), that is, $4.76 \text{ mM}^{-1} \text{ s}^{-1}$, indicating that Dy³⁺ ions in the core exhibit a negative impact on the T_1 contrast enhancement effects of Gd³⁺ in the shell.

In difference, the r_2 values of samples A₁, A₂, and A₃ are 1.38, 3.61, and $4.13 \text{ mM}^{-1} \text{ s}^{-1}$, respectively. Since the r_2 value of the reference sample was determined to be $6.49 \text{ mM}^{-1} \text{ s}^{-1}$, the increase of r_2 value against the particle size as a consequence of shell coating can be explained by the increasing amount of magnetic RE ions.

Relaxivities of Core–Shell–Shell Particles with Different Spacers. To further investigate the interaction between Dy³⁺ and Gd³⁺, the composition of the first shell, denoted as spacer layer hereafter, was varied according to the polarizability of RE ions involved, for example, Er³⁺ and Y³⁺. For comparing with NaDyF₄@NaGdF₄@NaGdF₄:Yb,Er, NaDyF₄@NaErF₄@NaGdF₄:Yb,Er (sample B₃) and NaDyF₄@NaYF₄@NaGdF₄:Yb,Er (sample C₃) nanoparticles were synthesized with similar procedures. The TEM images of samples B₃ and C₃ (Figure 3) show that they are similar short nanorods with

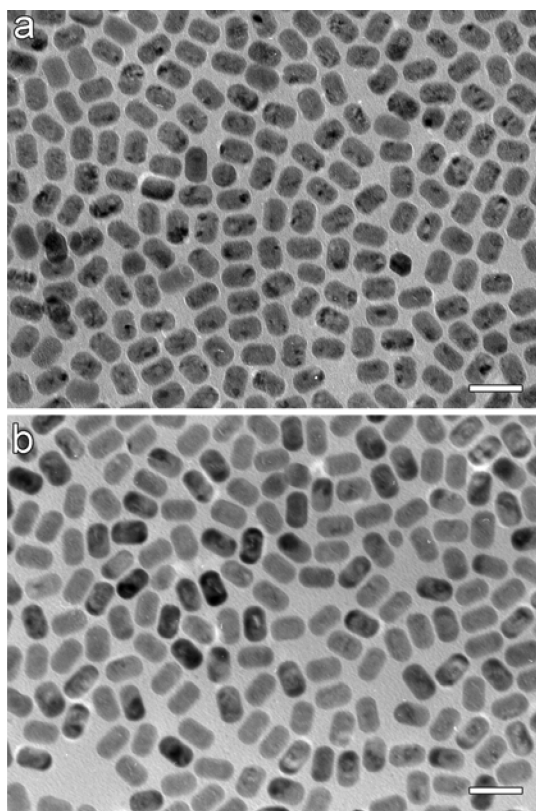


Figure 3. TEM images of NaDyF₄@NaErF₄@NaGdF₄:Yb,Er (denoted as sample B₃) (a) and NaDyF₄@NaYF₄@NaGdF₄:Yb,Er (denoted as sample C₃) (b) nanocrystals. The scale bars embedded in the TEM images correspond to 50 nm.

comparable sizes, that is, $21.6 \pm 1.5 \times 32.5 \pm 1.3 \text{ nm}$ (sample B₃) and $20.5 \pm 1.3 \times 36.4 \pm 1.8 \text{ nm}$ (sample C₃). In these two samples, the thicknesses of the NaErF₄ and NaYF₄ layers were calculated to be 2.2 and 1.9 nm, respectively. DLS measurement shown in Figure S2 reveals that both samples B₃ and C₃ present a single scattering peak locating at about 50.7 nm after being transferred into water, similar to sample A₃. The room-temperature magnetization curves shown in Figure S3 suggest that the core–shell–shell structured NaDyF₄@NaYF₄@NaGdF₄:Yb,Er nanocrystals are paramagnetic similar to NaDyF₄ and NaGdF₄ nanocrystals, even though they contain nonmagnetic Y³⁺.

The experimental data of longitudinal and transverse relaxivity measurements are shown in Figure 4. The relaxivity

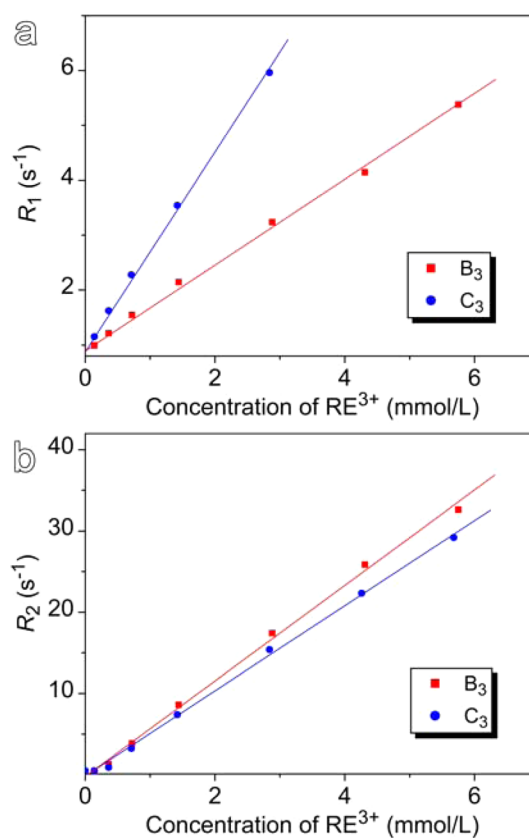


Figure 4. R_1 (a) and R_2 (b) of water protons plotted against the total molar concentration of magnetic RE ions in aqueous solution of samples B₃ and C₃. The solid lines are their corresponding linear fittings.

values of samples B₃ and C₃ together with sample A₃ are listed in Table 1. It is noteworthy that all the relaxivity values presented in the current study were calculated according to the total molar concentration of magnetic RE ions. It is therefore understandable for these seemingly lower values compared with previously reported ones extracted by separating the contribution of magnetic ions to either r_1 or r_2 of T_1/T_2 dual-

Table 1. Relaxivity Values of Samples A₃, B₃, and C₃

sample	r_1 ($\text{mM}^{-1} \text{ s}^{-1}$)	r_2 ($\text{mM}^{-1} \text{ s}^{-1}$)
A ₃	0.50	4.13
B ₃	0.78	5.88
C ₃	1.82	5.24

modality contrast agents.^{6,26,27} The current calculation method is more reliable for disclosing the interactions between the T_1 and T_2 components mediated by the spacer layer. Although the extracted r_2 values are very similar for A₃, B₃, and C₃, the r_1 values presented a clearly increasing trend, i.e., $r_1(\text{A}_3) < r_1(\text{B}_3) < r_1(\text{C}_3)$, which supports that the spacer composition can efficiently mediate the interactions between the Dy³⁺ in the core and the Gd³⁺ in the shell.

DISCUSSION

To understand the underlying mechanism governing the above-mentioned variations in the relaxometric properties of the core–shell–shell nanoparticles, the theory of longitudinal relaxivity is discussed below first.

Longitudinal relaxation rate (R_1) enhancement of water protons induced by paramagnetic RE nanoparticles involves inner-sphere (IS) and outer-sphere (OS) contributions.¹⁴ The inner-sphere contribution originates from the chemical exchange of the water molecules between the primary coordination sphere of the paramagnetic metal ions (or any hydration site near the metal) and the bulk solvent, while the outer-sphere contribution comes from the random translational diffusion of water molecules near the metal ions.

To put it simply, the inner-sphere longitudinal relaxation rate is mainly composed of contributions from the dipolar (R_{1D}^{IS}) and Curie (R_{1C}^{IS}) relaxations, which can be described by Solomon–Bloembergen equations:^{28,29}

$$R_{1D}^{\text{IS}} = \frac{2}{15} \left(\frac{\mu_0}{4\pi} \right)^2 \gamma_1^2 \mu_{\text{eff}}^2 \frac{1}{r^6} \left[\frac{3\tau_C}{1 + \omega_1^2 \tau_C^2} + \frac{7\tau_C}{1 + \omega_S^2 \tau_C^2} \right] \quad (1)$$

$$R_{1C}^{\text{IS}} = \frac{2}{5} \left(\frac{\mu_0}{4\pi} \right)^2 \gamma_1^2 \mu_C^2 \frac{1}{r^6} \left[\frac{3\tau_{CC}}{1 + \omega_1^2 \tau_{CC}^2} \right] \quad (2)$$

In the above equations, μ_0 is the permeability of vacuum, γ_1 is the proton gyromagnetic ratio, μ_{eff} is the effective magnetic moment of the RE ions ($\mu_{\text{eff}} = \mu_B g_J (J(J+1))^{1/2}$), μ_B is the Bohr magneton, g_J is the Landé factor, J is the quantum number of the total spin, μ_C is the Curie moment ($\mu_C = \mu_{\text{eff}}^2 B_0 / 3k_B T$), B_0 is the intensity of the static magnetic field, k_B is the Boltzmann constant, r is the distance between RE³⁺ and the RE-bound water protons, ω_1 and ω_S are the angular precession frequencies of proton and electron, respectively, τ_C is the correlation time modulating the dipolar interaction, and τ_{CC} is the correlation time for the Curie contribution. τ_C and τ_{CC} can be expressed as

$$\tau_C^{-1} = \tau_S^{-1} + \tau_R^{-1} + \tau_M^{-1} \quad (3)$$

$$\tau_{CC}^{-1} = \tau_R^{-1} + \tau_M^{-1} \quad (4)$$

τ_S is the electronic relaxation time, τ_M is the residence lifetime of the bound water, and τ_R is the rotational correlation time.

In the current study, samples A₃, B₃, C₃, and the reference sample have similar sizes, shapes, composition of the outermost layer, and surface coating as well; therefore factors except for correlation times (τ_S , τ_M , and τ_R) can be excluded when comparing their longitudinal relaxivities. In general, τ_S is positively correlated with longitudinal relaxivity, but limited by the value of τ_M or τ_R .¹⁴ For PEGylated NaREF₄ nanoparticles, τ_M can be ignored because it is usually significantly longer than τ_R and τ_S .³⁰ Because of the rather comparable size and surface coating, τ_R ($\tau_R = 4\pi a^3 \eta / 3k_B T$, η is viscosity of the medium, a is radius of particles) is also similar among these samples.

Therefore, it can be deduced that τ_S plays an important role in the inner-sphere R_1 .

The outer-sphere longitudinal relaxation rate also consists of a dipolar term modulated by the electronic relaxation time τ_S and a Curie term modulated by the translational correlation time τ_d ($\tau_d = d^2/D$, where d is the distance of closest approach of a water proton to the RE³⁺ center and D is the relative diffusion constant).^{31,32}

$$R_{1D}^{\text{OS}} = C_1 \mu_0^2 \gamma_1^2 \mu_B^2 g_J^2 \frac{M}{dD} [3j_D(\omega_1, \tau_d, \tau_S) + 7j_D(\omega_S, \tau_d, \tau_S)] \quad (5)$$

$$R_{1C}^{\text{OS}} = C_2 \mu_0^2 \gamma_1^2 \mu_B^2 g_J^2 \frac{M}{dD} \mu_C^2 [j_C(\omega_1, \tau_d)] \quad (6)$$

Similarly, the influence of τ_d can be excluded because of the similar composition of the outermost layer and surface coating. Thus, τ_S becomes the major factor herein for understanding the interaction between Dy³⁺ and Gd³⁺ as well as the function of the spacer layer. To further illuminate the intrinsic mechanism, the theory about magnetic field dependence of τ_S in solutions developed by Bloembergen and Morgan is shown below:²⁹

$$\frac{1}{\tau_S} = B \left[\frac{\tau_V}{1 + \omega_S^2 \tau_V^2} + \frac{4\tau_V}{1 + 4\omega_S^2 \tau_V^2} \right] \quad (7)$$

In eq 7, the constant B is related to the magnitude of the transient zero-field-splitting (ZFS), and τ_V is the correlation time to characterize the fluctuation causing the transient ZFS. Even though this theory is not totally valid when the static ZFS is not zero as in this work, this theory can still be applied to express the ZFS dependence of τ_S . The relationship between ZFS and τ_S is thought to be general: an increase in ZFS will lead to shorter τ_S and reduced relaxivity.¹⁴ The contribution to ZFS includes two parts: the main part arises from the spin–orbital coupling and the other essentially negligible part is from the direct dipolar spin–spin interaction. Therefore, the electron configurations determine the magnitude of τ_S and further influence the r_1 , which explains the difference between the relaxivities of Dy³⁺ and Gd³⁺. As well-known that Gd³⁺ has an isotropic electronic ground state (⁸S_{7/2}) and its half-filled f-orbital with seven unpaired electrons has no net orbital momentum, which results in a nearly zero spin–orbital interaction and little ZFS. As a result, τ_S of Gd³⁺ is relatively long, around 4–5 orders of magnitude longer than Dy³⁺ whose f-electrons distributed among f-orbital with large spin–orbital interaction and ZFS.^{14,33,34} Thus, r_1 value of Dy³⁺ is significantly lower than that of Gd³⁺.

The polarizability of Gd³⁺ is stronger than that of Dy³⁺; in principle, the electron clouds of Gd³⁺ ions may be distorted through electron cloud coupling with adjacent Dy³⁺ in core–shell–shell nanoparticles. Consequently, the isotropic electronic ground state of Gd³⁺ in the shell becomes anisotropic and the spin–orbital interaction arises, which leads to the increase of the magnitude of ZFS and the decrease of τ_S . The above results clearly revealed that all the core–shell–shell samples with NaDyF₄ as cores showed reduced r_1 value in comparison with the reference sample, which strongly support that Dy³⁺ can affect the T_1 effect by distorting the electron clouds of adjacent Gd³⁺ in the core–shell–shell particles.

Regarding the impact of the spacer layer on the relaxometric properties, Gd³⁺, Er³⁺, and Y³⁺ show a decreased tendency toward electron cloud distortion. Thus, the spacer layer of

NaYF₄ is more efficient to block the distortion effect between Dy³⁺ and Gd³⁺. Consequently, the NaDyF₄@NaYF₄@NaGdF₄:Yb,Er nanoparticles exhibited the highest longitudinal relaxivity among all core–shell–shell particles with different spacer compositions, even though the disturbance of NaDyF₄ to r_1 was not completely suppressed.

To further confirm this explanation, the upconversion luminescence arising from the codoping of Yb³⁺ and Er³⁺ was studied. Because the concentration of activator Er³⁺ is strongly related to the luminescence intensity of the upconversion nanoparticles, samples A₃ and C₃ were carefully compared as they two have comparable content of Er³⁺. As shown in Figure 5, sample C₃ exhibits much higher luminescence intensity than

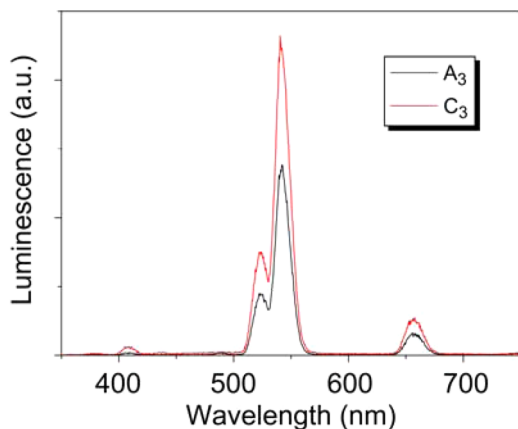


Figure 5. Normalized upconversion luminescence spectra of samples A₃ and C₃ recorded upon excitation by a CW 980 nm laser.

sample A₃, with normalized concentration of Er³⁺. Dy³⁺ is known as a quencher of upconversion luminescence of Er³⁺ since the excitation energy can transfer to the lower electronic energy states of Dy³⁺ through electron cloud coupling and then decays through nonradiative transitions.³⁵ The core–shell–shell structure spatially confines the activator and quencher in different layers, and the spacer regulates the energy exchange between the core and the outer shell, which is essential for eliminating deleterious cross-relaxation. As shown in Figure 5, when NaYF₄ is involved to separate Dy³⁺ in the core and RE³⁺ in the outer shell, the upconversion luminescence is sufficiently enhanced, which supports that the NaYF₄ spacer layer can efficiently reduce the interactions between Dy³⁺ and Gd³⁺ for achieving high-performance magnetic/upconversion particles for T₁/T₂ MR and optical imaging applications.

Following the above study, NaDyF₄@NaYF₄@NaGdF₄:Yb,Er nanocrystal with a thicker NaYF₄ spacer layer was designed for more effectively enhancing the blocking effect and a new series of samples including core NaDyF₄, core–shell NaDyF₄@NaYF₄, and core–shell–shell NaDyF₄@NaYF₄@NaGdF₄:Yb,Er nanocrystals were prepared and denoted as samples D₁, D₂, and D₃, respectively. The TEM images of samples D₁ and D₂ are shown in Figure S3 and a representative image of sample D₃ together with the data of relaxometric measurements are shown in Figure 6. Careful measurements revealed that the average sizes of samples D₁, D₂, and D₃ were 19.9 ± 0.8, 27.0 ± 1.6 × 39.8 ± 2.0, and 36.6 ± 2.1 × 54.5 ± 1.5 nm, respectively, based on the thickness of the spacer layer estimated to be around 3.5 nm, much larger than that in sample C₃ (1.9 nm). Consequently, the r_1 value is increased up to 2.47 mM⁻¹ s⁻¹ from 1.82 mM⁻¹ s⁻¹ for sample C₃.

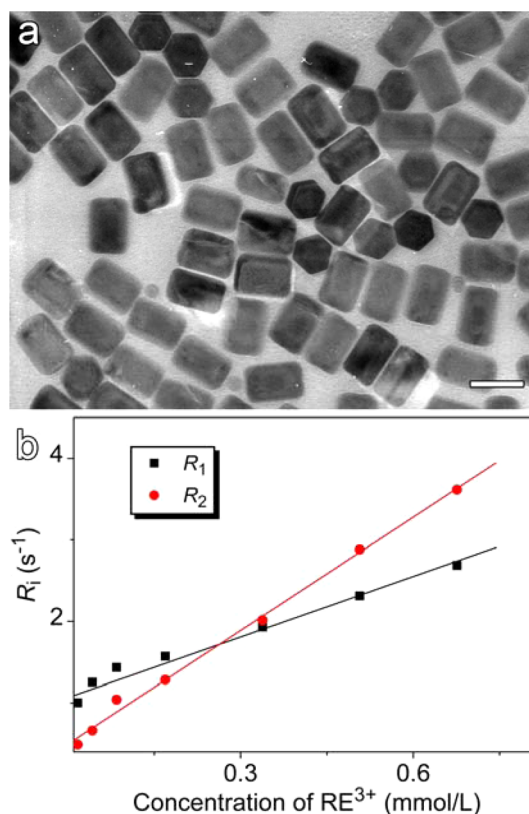


Figure 6. (a) TEM image of NaDyF₄@NaYF₄@NaGdF₄:Yb,Er nanocrystals with thicker spacer layer (denoted as sample D₃). The scale bar embedded in the TEM image corresponds to 50 nm. (b) R_1 and R_2 of water protons plotted against the total molar concentration of magnetic RE ions in aqueous solution of sample D₃ together with their corresponding linear fittings.

CONCLUSIONS

In summary, core–shell–shell structured NaDyF₄@NaREF₄@NaGdF₄:Yb,Er (RE = Gd, Er, Y) nanoparticles have been prepared through seed-mediated growth to integrate T₁ signal units (Gd³⁺) and T₂ signal units (Dy³⁺). By variation of the NaREF₄ spacer layer, the interactions between Gd³⁺ and Dy³⁺ have been systematically investigated. Careful relaxometric studies in combination with theoretical analysis suggest that the strong coupling interaction between the electron clouds of Dy³⁺ and Gd³⁺ decreases the r_1 value of the system. But this interaction can be manipulated by the spacer layer NaREF₄ containing RE element with weak distortion ability of electron cloud such as Y³⁺ to effectively suppress the negative impact of Dy³⁺, which is further supported by upconversion luminescence studies. In addition, a thicker NaYF₄ spacer layer is also found to be favorable for achieving higher r_1 value. Although the negative impact of Dy³⁺ on both r_1 and upconversion luminescence efficiency are not completely ruled out with NaYF₄ spacer layer, the current study offers a reliable understanding for tailoring the relaxometric properties and upconversion luminescent properties of RE nanoparticles that are potentially useful for biomedical imaging applications.

ASSOCIATED CONTENT

Supporting Information

Electron diffraction patterns of samples A₁, A₂, and A₃. The hydrodynamic size distribution profiles of samples B₃ and C₃. Room-temperature magnetization curves of NaDyF₄, NaGdF₄,

and NaDyF₄@NaYF₄@NaGdF₄:Yb,Er nanocrystals. TEM images of the core particles for sample D₃. The Supporting Information is available free of charge on the ACS Publications website at DOI: 10.1021/acs.chemmater.5b02875.

(PDF)

AUTHOR INFORMATION

Corresponding Authors

*E-mail: gaomy@iccas.ac.cn. Fax: +86 10 8261 3214.

*E-mail: liuchy@iccas.ac.cn

Notes

The authors declare no competing financial interest.

ACKNOWLEDGMENTS

This work was financially supported by the National Basic Research Program of China (2011CB935800), NSFC (21403250, 21203211, 81471726, 21321063), and CAS (CMS-PY-201309, CMS-PY-201314).

REFERENCES

- (1) Bottrill, M.; Kwok, L.; Long, N. J. Lanthanides in magnetic resonance imaging. *Chem. Soc. Rev.* **2006**, *35*, 557–571.
- (2) Na, H. B.; Song, I. C.; Hyeon, T. Inorganic Nanoparticles for MRI Contrast Agents. *Adv. Mater.* **2009**, *21*, 2133–2148.
- (3) Qin, J.; Laurent, S.; Jo, Y. S.; Roch, A.; Mikhaylova, M.; Bhujwalla, Z. M.; Muller, R. N.; Muhammed, M. A High-Performance Magnetic Resonance Imaging T₂ Contrast Agent. *Adv. Mater.* **2007**, *19*, 1874–1878.
- (4) Kenouche, S.; Larionova, J.; Bezzi, N.; Guari, Y.; Bertin, N.; Zanca, M.; Lartigue, L.; Cieslak, M.; Godin, C.; Morrot, G.; Goze-Bac, C. NMR investigation of functionalized magnetic nanoparticles Fe₃O₄ as T₁–T₂ contrast agents. *Powder Technol.* **2014**, *255*, 60–65.
- (5) Terreno, E.; Castelli, D. D.; Viale, A.; Aime, S. Challenges for molecular magnetic resonance imaging. *Chem. Rev.* **2010**, *110*, 3019–3042.
- (6) Choi, J. S.; Lee, J. H.; Shin, T. H.; Song, H. T.; Kim, E. Y.; Cheon, J. Self-Confirming “AND” Logic Nanoparticles for Fault-Free MRI. *J. Am. Chem. Soc.* **2010**, *132*, 11015–11017.
- (7) Shin, T. H.; Choi, J. S.; Yun, S.; Kim, I. S.; Song, H. T.; Kim, Y.; Park, K. I.; Cheon, J. T₁ and T₂ Dual-Mode MRI Contrast Agent for Enhancing Accuracy by Engineered Nanomaterials. *ACS Nano* **2014**, *8*, 3393–3401.
- (8) Zhou, Z. J.; Huang, D. T.; Bao, J. F.; Chen, Q. L.; Liu, G.; Chen, Z.; Chen, X. Y.; Gao, J. H. A Synergistically Enhanced T₁–T₂ Dual-Modal Contrast Agent. *Adv. Mater.* **2012**, *24*, 6223–6228.
- (9) Tromsdorf, U. I.; Bruns, O. T.; Salmen, S. C.; Beisiegel, U.; Weller, H. A Highly Effective, Nontoxic T₁ MR Contrast Agent Based on Ultrasmall PEGylated Iron Oxide Nanoparticles. *Nano Lett.* **2009**, *9*, 4434–4440.
- (10) Seo, W. S.; Lee, J. H.; Sun, X.; Suzuki, Y.; Mann, D.; Liu, Z.; Terashima, M.; Yang, P. C.; McConnell, M. V.; Nishimura, D. G.; Dai, H. FeCo/graphitic-shell nanocrystals as advanced magnetic-resonance-imaging and near-infrared agents. *Nat. Mater.* **2006**, *5*, 971–976.
- (11) Zeng, J. F.; Jing, L. H.; Hou, Y.; Jiao, M. X.; Qiao, R. R.; Jia, Q. J.; Liu, C. Y.; Fang, F.; Lei, H.; Gao, M. Y. Anchoring Group Effects of Surface Ligands on Magnetic Properties of Fe₃O₄ Nanoparticles: Towards High Performance MRI Contrast Agents. *Adv. Mater.* **2014**, *26*, 2694–2698.
- (12) Huang, C. C.; Tsai, C. Y.; Sheu, H. S.; Chuang, K. Y.; Su, C. H.; Jeng, U. S.; Cheng, F. Y.; Su, C. H.; Lei, H. Y.; Yeh, C. S. Enhancing Transversal Relaxation for Magnetite Nanoparticles in MR Imaging Using Gd³⁺-Chelated Mesoporous Silica Shells. *ACS Nano* **2011**, *5*, 3905–3916.
- (13) Yang, H.; Zhuang, Y.; Sun, Y.; Dai, A.; Shi, X.; Wu, D.; Li, F.; Hu, H.; Yang, S. Targeted dual-contrast T₁- and T₂-weighted magnetic resonance imaging of tumors using multifunctional gadolinium-labeled superparamagnetic iron oxide nanoparticles. *Biomaterials* **2011**, *32*, 4584–4593.
- (14) Lauffer, R. B. Paramagnetic metal complexes as water proton relaxation agents for NMR imaging: theory and design. *Chem. Rev.* **1987**, *87*, 901–927.
- (15) Caravan, P.; Ellison, J. J.; McMurry, T. J.; Lauffer, R. B. Gadolinium(III) Chelates as MRI Contrast Agents: Structure, Dynamics, and Applications. *Chem. Rev.* **1999**, *99*, 2293–2352.
- (16) Liu, C. Y.; Hou, Y.; Gao, M. Y. Are Rare-Earth Nanoparticles Suitable for In Vivo Applications? *Adv. Mater.* **2014**, *26*, 6922–6932.
- (17) Evanics, F.; Diamente, P. R.; van Veggel, F. C. J. M.; Stanisz, G. J.; Prosser, R. S. Water-Soluble GdF₃ and GdF₃/LaF₃ Nanoparticles Physical Characterization and NMR Relaxation Properties. *Chem. Mater.* **2006**, *18*, 2499–2505.
- (18) Bridot, J. L.; Faure, A. C.; Laurent, S.; Rivière, C.; Billotey, C.; Hiba, B.; Janier, M.; Jossierand, V.; Coll, J. L.; Vander Elst, L.; Muller, R.; Roux, S.; Perriat, P.; Tillement, O. Hybrid Gadolinium Oxide Nanoparticles: Multimodal Contrast Agents for in Vivo Imaging. *J. Am. Chem. Soc.* **2007**, *129*, 5076–5084.
- (19) Hou, Y.; Qiao, R. R.; Fang, F.; Wang, X. X.; Dong, C. Y.; Liu, K.; Liu, C. Y.; Liu, Z. F.; Lei, H.; Wang, F.; Gao, M. Y. NaGdF₄ Nanoparticle-Based Molecular Probes for Magnetic Resonance Imaging of Intraperitoneal Tumor Xenografts in Vivo. *ACS Nano* **2013**, *7*, 330–338.
- (20) Norek, M.; Peters, J. A. MRI contrast agents based on dysprosium or holmium. *Prog. Nucl. Magn. Reson. Spectrosc.* **2011**, *59*, 64–82.
- (21) Das, G. K.; Johnson, N. J. J.; Cramen, J.; Blasiak, B.; Latta, P.; Tomanek, B.; van Veggel, F. C. J. M. NaDyF₄ Nanoparticles as T₂ Contrast Agents for Ultrahigh Field Magnetic Resonance Imaging. *J. Phys. Chem. Lett.* **2012**, *3*, 524–529.
- (22) Kattel, K.; Park, J. Y.; Xu, W.; Kim, H. G.; Lee, E. J.; Bony, B. A.; Heo, W. C.; Jin, S.; Baeck, J. S.; Chang, Y.; Kim, T. J.; Bae, J. E.; Chae, K. S.; Lee, G. H. Paramagnetic dysprosium oxide nanoparticles and dysprosium hydroxide nanorods as T₂ MRI contrast agents. *Biomaterials* **2012**, *33*, 3254–3261.
- (23) Liu, C. Y.; Gao, Z. Y.; Zeng, J. F.; Hou, Y.; Fang, F.; Li, Y.; Qiao, R. R.; Shen, L.; Lei, H.; Yang, W. S.; Gao, M. Y. Magnetic/Upconversion Fluorescent NaGdF₄:Yb,Er Nanoparticle-Based Dual-Modal Molecular Probes for Imaging Tiny Tumors in Vivo. *ACS Nano* **2013**, *7*, 7227–7240.
- (24) Qiao, R. R.; Liu, C. H.; Liu, M. H.; Hu, H.; Liu, C. Y.; Hou, Y.; Wu, K. C.; Lin, Y. N.; Liang, J. M.; Gao, M. Y. Ultrasensitive in Vivo Detection of Primary Gastric Tumor and Lymphatic Metastasis Using Upconversion Nanoparticles. *ACS Nano* **2015**, *9*, 2120–2129.
- (25) Wang, F.; Han, Y.; Lim, C. S.; Lu, Y.; Wang, J.; Xu, J.; Chen, H.; Zhang, C.; Hong, M.; Liu, X. Simultaneous phase and size control of upconversion nanocrystals through lanthanide doping. *Nature* **2010**, *463*, 1061–1065.
- (26) Zhou, J.; Lu, Z.; Shan, G.; Wang, S.; Liao, Y. Gadolinium complex and phosphorescent probe-modified NaDyF₄ nanorods for T₁- and T₂-weighted MRI/CT/phosphorescence multimodality imaging. *Biomaterials* **2014**, *35*, 368–377.
- (27) Xiao, N.; Gu, W.; Wang, H.; Deng, Y. L.; Shi, X.; Ye, L. T₁–T₂ dual-modal MRI of brain gliomas using PEGylated Gd-doped iron oxide nanoparticles. *J. Colloid Interface Sci.* **2014**, *417*, 159–165.
- (28) Solomon, I. Relaxation Processes in a System of Two Spins. *Phys. Rev.* **1955**, *99*, 559–565.
- (29) Bloembergen, N.; Morgan, L. O. Proton Relaxation Times in Paramagnetic Solutions. Effects of Electron Spin Relaxation. *J. Chem. Phys.* **1961**, *34*, 842–850.
- (30) Bertini, I.; Capozzi, F.; Luchinat, C.; Nicastro, G.; Xia, Z. Water proton relaxation for some lanthanide aqua ions in solution. *J. Phys. Chem.* **1993**, *97*, 6351–6354.
- (31) Hwang, L. P.; Freed, J. H. Dynamic effects of pair correlation functions on spin relaxation by translational diffusion in liquids. *J. Chem. Phys.* **1975**, *63*, 4017–4025.

(32) Freed, J. H. Dynamic effects of pair correlation functions on spin relaxation by translational diffusion in liquids. II. Finite jumps and independent T_1 processes. *J. Chem. Phys.* **1978**, *68*, 4034–4037.

(33) Aime, S.; Barbero, L.; Botta, M.; Ermondi, G. Determination of metal-proton distances and electronic relaxation times in lanthanide complexes by nuclear magnetic resonance spectroscopy. *J. Chem. Soc., Dalton Trans.* **1992**, 225–228.

(34) Banci, L.; Bertini, I.; Luchinat, C. ^1H NMRD studies of solutions of paramagnetic metal ions in ethyleneglycol. *Inorg. Chim. Acta* **1985**, *100*, 173–181.

(35) Dong, H.; Sun, L. D.; Yan, C. H. Basic understanding of the lanthanide related upconversion emissions. *Nanoscale* **2013**, *5*, 5703–5714.